

Decoherence of V_B^- spin defects in monoisotopic hexagonal boron nitride

A. Haykal,¹ R. Tanos,¹ N. Minotto,¹ A. Durand,¹ F. Fabre,¹ J. Li,² J. H. Edgar,²
V. Ivady,^{3,4} A. Gali,^{5,6} T. Michel,¹ A. Dréau,¹ B. Gil,¹ G. Cassabois,¹ and V. Jacques¹

¹Laboratoire Charles Coulomb, Université de Montpellier and CNRS, 34095 Montpellier, France

²Tim Taylor Department of Chemical Engineering,

Kansas State University, Manhattan, Kansas 66506, USA

³Max Planck Institute for the Physics of Complex Systems, Nöthnitzer Straße 38, 01187 Dresden, Germany

⁴Department of Physics, Linköping University, SE-581 83 Linköping, Sweden

⁵Wigner Research Centre for Physics, P.O. Box 49, H-1525 Budapest, Hungary

⁶Department of Atomic Physics, Budapest University of Technology and Economics, Budafoki út 8., H-1111 Budapest, Hungary

(Dated: December 21, 2021)

Spin defects in hexagonal boron nitride (hBN) are promising quantum systems for the design of flexible two-dimensional quantum sensing platforms. Here we rely on hBN crystals isotopically enriched with either ^{10}B or ^{11}B to investigate the isotope-dependent properties of a spin defect featuring a broadband photoluminescence signal in the near infrared. By analyzing the hyperfine structure of the spin defect while changing the boron isotope, we first unambiguously confirm that it corresponds to the negatively-charged boron-vacancy center (V_B^-). We then show that its spin coherence properties are slightly improved in ^{10}B -enriched samples. This is supported by numerical simulations employing cluster correlation expansion methods, which reveal the importance of the hyperfine Fermi contact term for calculating the coherence time of point defects in hBN. Using cross-relaxation spectroscopy, we finally identify dark electron spin impurities as an additional source of decoherence. This work provides new insights into the properties of V_B^- spin defects, which are valuable for the future development of hBN-based quantum sensing foils.

Optically-active point defects in semiconductors are currently attracting intense research attention owing to prospective applications in the growing field of quantum technologies [1]. These defects, that feature localized electronic states with energy levels deeply buried inside the bandgap of the host material, behave as artificial atoms with efficient optical transitions. Importantly, the electronic spin of the defect can offer a fertile quantum resource for the development of a wide variety of applications. Besides its use as a quantum bit for the realization of advanced quantum information protocols [2–4], the electronic spin state can also be exploited for quantum sensing purposes, by taking advantage of its extreme sensitivity to external perturbations such as magnetic and electric fields, pressure or temperature [5]. In this context, the nitrogen-vacancy (NV) defect in diamond is undoubtedly the most advanced solid-state quantum sensing platform, which has already found numerous applications in condensed matter physics and life sciences [6–8]. However, the search for alternative material platforms that could expand the range of quantum sensing functionalities offered by diamond remains very active worldwide [9]. Along this research line, a particular attention is currently being paid to layered van der Waals crystals because such materials promise the design of flexible, atomically-thin quantum sensing foils [10, 11].

Among the broad variety of layered van der Waals crystals, hexagonal boron nitride (hBN) is an ideal material for hosting optically-active spin defects owing to its large bandgap (~ 6 eV) [12]. During the last years, many papers have reported the isolation of individual defects in hBN, showing very bright optical emission and perfect

photostability, even at ambient conditions [13–17]. However, the detection of the electron spin state associated with these point defects has long remained a missing ingredient towards the development of quantum sensors. This gap has been recently filled with the demonstration of optically detected magnetic resonance on two different types of defects, which have been tentatively assigned to negatively-charged boron vacancy centers [18, 19] and carbon-related impurities [20–22]. Unambiguously identifying the microscopic structure of optically-active spin defects remains however a highly difficult task given the large number of potential candidates, which can involve extrinsic substitutional or interstitial impurities as well as complex assemblies of vacancies and antisite defects. Density functional theory is a powerful tool to reduce the number of possible atomic structures through *ab initio* calculations of defect properties such as formation energies, charge state transition levels, photoluminescence (PL) spectra or electron spin densities [23–28]. On the experimental side, valuable informations can be obtained by analysing the hyperfine structure of the spin defect [18, 21], which results from its interaction with neighboring nuclear spin species.

In hBN, each lattice site is occupied by an atom with a non-zero nuclear spin, in contrast to other materials such as diamond or silicon carbide. Nitrogen naturally occurs as the ^{14}N isotope with a nuclear spin $I = 1$ (99.6% natural abundance), while boron has two stable isotopes, ^{11}B with a nuclear spin $I = 3/2$ (80% natural abundance) and ^{10}B with a nuclear spin $I = 3$ (20% natural abundance). To date, all the studies of spin defects in hBN were performed on crystals with the natural con-

tent of boron isotopes [18–22], making the interpretation of hyperfine spectra a difficult task [28]. In this work, we circumvent this problem by employing hBN crystals containing a single boron isotope. Using such monoisotopic crystals, we focus our study on a spin defect featuring a broadband PL signal centered at a wavelength of 800 nm. The analysis of its hyperfine structure while changing the boron isotope confirms unambiguously that this defect corresponds to the negatively-charged boron-vacancy center (V_{B}^-). We then investigate the spin coherence properties of V_{B}^- centers hosted in monoisotopic hBN crystals. We observe a slight increase of the spin coherence time T_2 in ^{10}B -enriched samples, which is supported by numerical simulations using cluster correlation expansion methods. Using cross-relaxation spectroscopy, we finally identify dark electron spin impurities as an additional source of decoherence for the V_{B}^- center in hBN.

Monoisotopic, millimeter-sized $h^{10}\text{BN}$ and $h^{11}\text{BN}$ crystals were synthesized through the metal flux growth method described in Ref. [29], while using isotopically enriched boron powders with either ^{11}B (99.4%) or ^{10}B (99.2%). The resulting crystals were irradiated with thermal neutrons to produce point defects. Two different processes can lead to the creation of defects via neutron irradiation: either by damages produced by neutron scattering through the crystal or via neutron absorption leading to nuclear transmutation. The latter process strongly depends on the isotopic content of the hBN crystal. Indeed, the thermal neutron capture cross-sections of ^{11}B (~ 0.005 barn) and ^{14}N (~ 1.8 barn) are orders of magnitude smaller than that of ^{10}B (~ 3890 barn) [30]. As a result, neutron irradiation of the $h^{10}\text{BN}$ crystal likely creates boron vacancy-related defects through nuclear transmutation and introduces interstitial ^7Li atoms resulting from the fission of the ^{10}B isotope [30]. Conversely, the $h^{11}\text{BN}$ crystal is almost transparent to neutrons and point defects are solely created by neutron scattering. To partially compensate for the isotope-dependent efficiency of defect creation by neutron irradiation, the $h^{11}\text{BN}$ crystal was irradiated with a dose of $\sim 2.6 \times 10^{17}$ n cm^{-2} and the $h^{10}\text{BN}$ crystal with a smaller dose of $\sim 2.6 \times 10^{16}$ n cm^{-2} .

The monoisotopic content of our neutron-irradiated hBN crystals was first verified through Raman scattering spectroscopy. Figure 1(a) shows the Raman spectra recorded from the $h^{10}\text{BN}$ and $h^{11}\text{BN}$ crystals around the energy of the intralayer E_{2g} phonon mode that corresponds to the in-plane vibration of boron and nitrogen atoms [31]. The energy of this phonon mode is at 1358 cm^{-1} for $h^{11}\text{BN}$ and is shifted to 1394 cm^{-1} for $h^{10}\text{BN}$, as expected from the isotopic mass difference [32, 33]. The full-width at half maximum of the Raman line is around 4.5 cm^{-1} , attesting for the high crystalline quality of the hBN samples. This value is however slightly larger than that usually measured on similar crys-

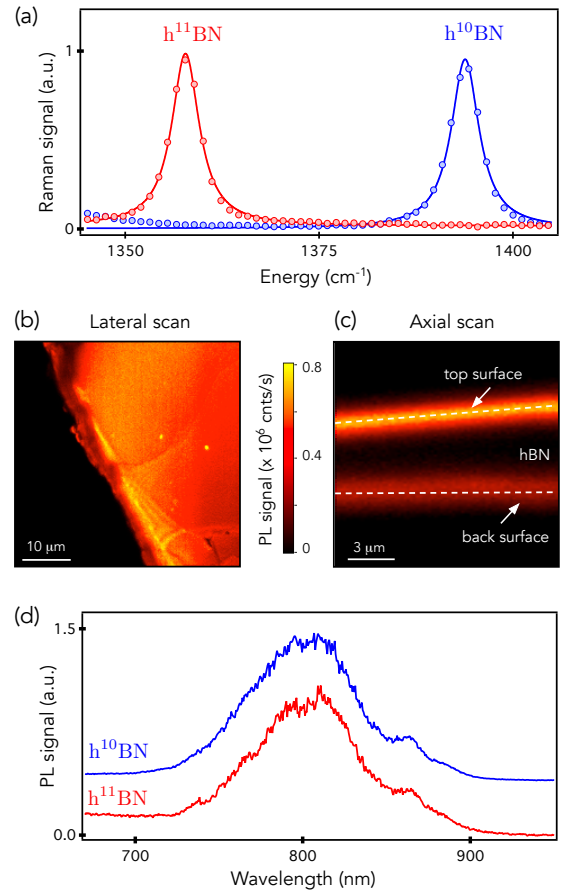


FIG. 1. **Optical properties of neutron-irradiated monoisotopic hBN crystals.** (a) Raman scattering spectra recorded at room temperature on the $h^{11}\text{BN}$ (red dots) and $h^{10}\text{BN}$ crystals (blue dots) after neutron irradiation. The solid lines are data fitting with Lorentzian functions. (b) Typical lateral PL raster scan of the $h^{10}\text{BN}$ crystals under green laser illumination with a power of 1 mW. (c) Axial confocal scan showing a high PL signal localized at the crystal surfaces. (d) PL spectra recorded from the $h^{11}\text{BN}$ (red) and $h^{10}\text{BN}$ crystals (blue). The data have been normalized and vertically shifted for the sake of clarity.

tals not subjected to neutron irradiation (~ 3 cm^{-1}) [32].

The PL properties were then analyzed with a scanning confocal microscope operating at ambient conditions. A laser excitation at 532 nm was focused onto the sample with a high numerical aperture microscope objective (NA=0.95) mounted on a three-axis piezoelectric scanner. The PL signal was collected by the same objective, focused in a $50\text{-}\mu\text{m}$ -diameter pinhole and finally directed either to a spectrometer or to a silicon avalanche photodiode operating in the single-photon counting regime. A lateral PL raster scan of the $h^{10}\text{BN}$ crystal is shown in Fig. 1(b). It reveals a uniform PL signal, which is characterized by a broadband emission spectrum centered around $\lambda \approx 800$ nm [Fig. 1(d)]. It was recently proposed to assign this emission line to negatively-charged boron-

vacancy centers (V_B^-) [18, 19, 26]. A similar PL signal was observed on the $h^{11}BN$ crystal [Fig. 1(d)], though with an intensity decreased by roughly one order of magnitude despite a larger neutron irradiation dose. This confirms that point defects are efficiently created through nuclear transmutation in the $h^{10}BN$ crystal. Interestingly, a confocal PL scan recorded along the depth of the crystal shows that optically-active defects are tightly localized at the sample surfaces [Fig. 1(c)]. Here the width of the hBN layer producing a PL signal is indeed limited by the longitudinal spatial resolution of the confocal microscope ($\sim 2 \mu m$). This may be due either to the efficient migration of vacancy-related defects towards the surfaces or, more likely, to the stabilization of their charge state in an optically-active configuration through a variation of the Fermi level close to the sample surface [34]. Although a precise understanding of this effect is beyond the scope of the present work, this is an important information for the future integration of exfoliated hBN layers doped with optically-active spin defects into van der Waals heterostructures.

The point defect associated with the emission line at $\lambda \approx 800$ nm exhibits very similar magneto-optical properties to those of the NV defect in diamond [18, 19]. It features a spin triplet ground state $S = 1$, that can be polarized through optical pumping, coherently manipulated with a microwave excitation, and readout by recording its spin-dependent PL signal. These properties enable the detection of electron spin resonances (ESR) by optical means [18, 19]. Optically-detected ESR spectra were recorded by monitoring the PL signal while sweeping the frequency of a microwave field applied through a copper microwire directly spanned on the sample surface. When the microwave frequency crosses a transition between the ground state electron spin sublevels, the magnetic resonance is evidenced as a drop of the PL signal. At zero external magnetic field, the ESR frequencies are given by $\nu_{\pm} = D \pm E$, where D and E denote the longitudinal and transverse zero-field splitting parameters, respectively. A typical ESR spectrum recorded at zero field on the $h^{10}BN$ crystal is displayed in Fig. 2(a). From this experiment, we infer $D = 3.47$ GHz and $E = 61 \pm 1$ MHz, in good agreement with previous works [18, 19]. Similar results were obtained for the $h^{11}BN$ crystal.

To investigate the hyperfine structure of the spin defect, a static magnetic field was applied along the c axis in order to shift the electron spin sublevels via the Zeeman effect and thus isolate a single ESR line in the spectrum [Fig. 2(a)]. The hyperfine structure recorded on the $h^{11}BN$ crystal is displayed in Fig. 2(b). Seven hyperfine lines can be resolved, with a characteristic splitting $\mathcal{A} \sim 44$ MHz. This structure is analogous to that observed in hBN crystals with a natural content of boron isotopes, that corresponds to 80% of ^{11}B [18, 19]. The same experiment was performed for spin defects hosted in the monoisotopic $h^{10}BN$ crystal, leading to a very similar

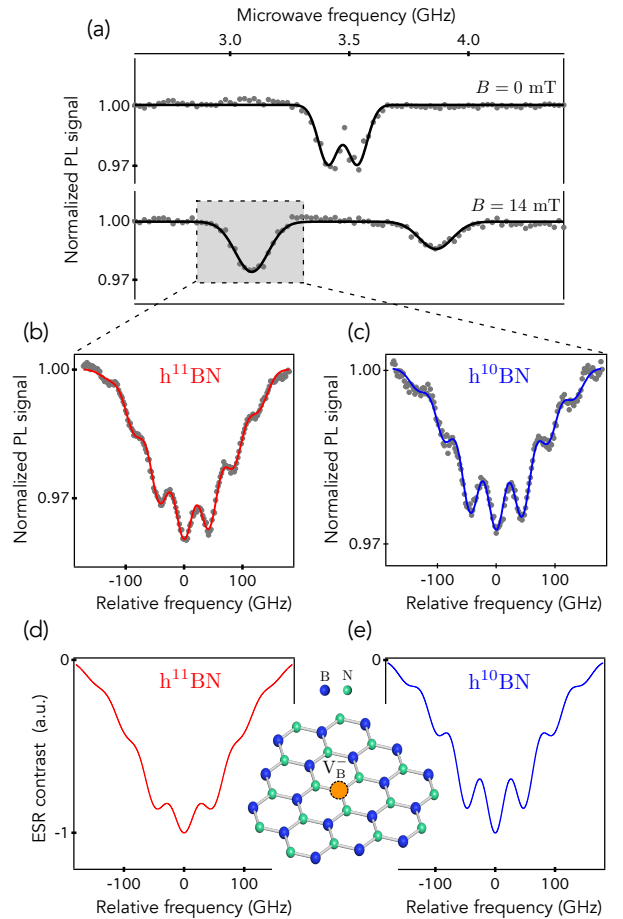


FIG. 2. **Analysis of the hyperfine structure.** (a) Optically-detected ESR spectra recorded on the $h^{10}BN$ crystal at zero field (top panel) and for a magnetic field $B = 14$ mT applied along the c axis, *i.e.* perpendicular to the sample surface. (b,c) Hyperfine structure of the ESR line measured in (b) $h^{11}BN$ and (c) $h^{10}BN$ crystals. The solid lines are data fitting with a sum of seven Gaussian functions. (d,e) Simulated hyperfine spectra of the V_B^- defect in hBN (see inset) obtained via the procedure described in the main text while using $\Delta_s = 30$ MHz. The inset shows the atomic structure of the V_B^- center in hBN .

hyperfine spectrum [Fig. 2(c)]. This observation unambiguously indicates that boron atoms are not involved in the seven-line structure of the hyperfine spectrum, and are therefore not localized at the first neighboring lattice sites of the spin defect. Considering the intrinsic nuclear spin species in hBN , the hyperfine structure can only be explained by the interaction of a central electronic spin with three equivalent ^{14}N nucleus ($I = 1$). This situation can be obtained either for a boron-vacancy center or for a substitutional impurity with zero nuclear spin localized at a boron site. This last possibility is ruled out because the studied spin defect is efficiently created in the $h^{10}BN$ crystal via neutron transmutation doping, which likely produces boron vacancy-related centers. We

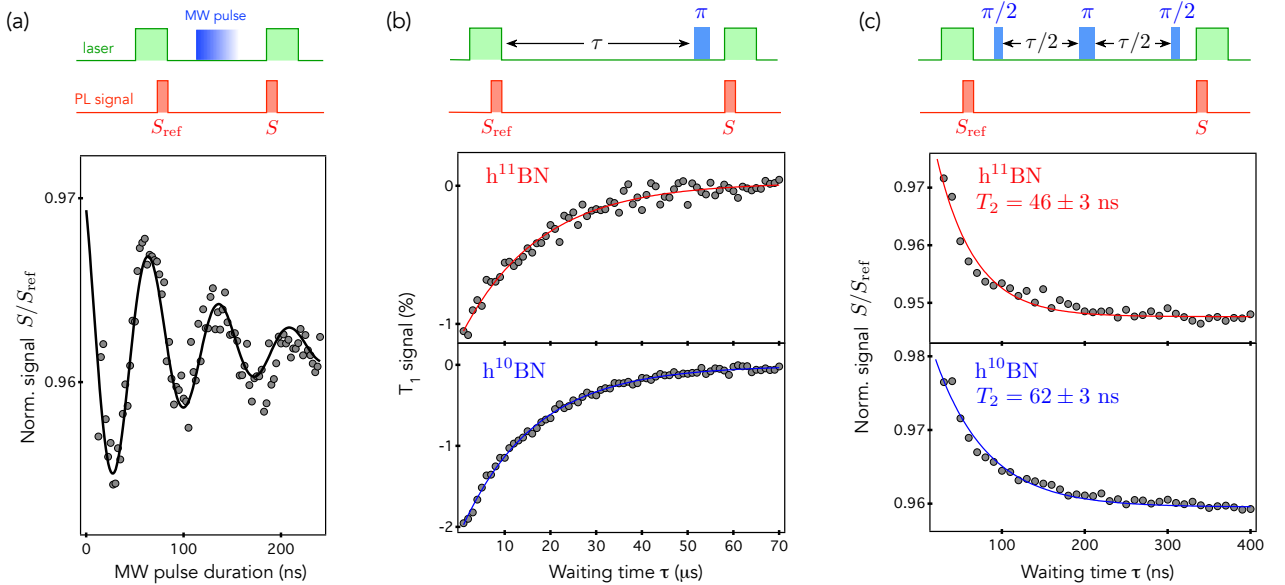


FIG. 3. **Spin coherence properties.** (a) Optically-detected Rabi oscillations of the V_B^- spin defects recorded by applying the experimental sequence shown in the top panel. The spin-dependent PL signal S is integrated at the beginning of the readout laser pulse and normalized by a reference signal S_{ref} , which corresponds to the steady-state PL signal measured at the end of the initialization laser pulse. (b) T_1 measurements in the two monoisotopic crystals. Here we plot the difference of the normalized PL signal S/S_{ref} measured with and without applying the resonant microwave π -pulse (see top panel). Solid lines are data fitting with an exponential decay, leading to $T_1 \sim 16 \mu\text{s}$ in both samples. (c) Measurement of the spin coherence time T_2 using a spin echo pulse sequence. Solid lines are data fitting with an exponential decay. All experiments are performed with a static magnetic field $B \sim 15 \text{ mT}$ applied along the c axis. The duration of the laser pulses is $8 \mu\text{s}$ with a power of 1 mW and the integration time window of S and S_{ref} is fixed to 300 ns .

conclude that the broad emission line centered at a wavelength of 800 nm in hBN corresponds to the V_B^- center, as proposed in recent experimental works [18, 19] and supported by *ab initio* theoretical calculations [26].

The hyperfine interaction of the V_B^- center with the six equivalent boron atoms placed in the second neighboring lattice sites cannot be detected and leads to a broadening of the ESR lines. At first glance, it might be surprising to observe similar linewidths in $h^{11}\text{BN}$ and $h^{10}\text{BN}$ crystals, because the ^{10}B isotope has a higher nuclear spin ($I = 3$) than ^{11}B ($I = 3/2$). This is due to the difference in nuclear gyromagnetic ratio between the two isotopes, $\gamma_n = 4.6 \text{ MHz/T}$ for ^{10}B and $\gamma_n = 13.7 \text{ MHz/T}$ for ^{11}B . Since the hyperfine coupling strength scales linearly with γ_n , it is reduced by a factor of three for ^{10}B , which compensates for the impact of a higher nuclear spin in the broadening of the ESR line. To illustrate further this effect, simple simulations of the ESR spectra were performed. An exact calculation using a direct diagonalisation of the spin Hamiltonian cannot be done with conventional computer resources given the large number of nuclear spins involved. We therefore rely on a simplified model for which we only consider the longitudinal component \mathcal{A}_{zz} of the hyperfine tensor. Here z denotes the quantization axis of V_B^- , which corresponds to the c -axis of the hBN crystal [18]. The hyperfine coupling constants were taken from the *ab initio* calculations reported

in Ref. [26]. The simulation includes (i) the three equivalent ^{14}N first-neighbors with $\mathcal{A}_{zz} = 47 \text{ MHz}$, (ii) the six second-neighbors boron atoms with $\mathcal{A}_{zz} = -4.6 \text{ MHz}$ (resp. -1.5 MHz) for ^{11}B (resp. ^{10}B), and (iii) six equivalent ^{14}N third-neighbors with $\mathcal{A}_{zz} = 4.5 \text{ MHz}$. After calculating the position of the hyperfine lines, a convolution was applied with a Gaussian profile to take into account the inhomogeneous broadening of the V_B^- electron spin transitions. The hyperfine spectra were simulated for various full-width at half maximum Δ_s of the Gaussian function. In Fig. 2(d-e), we display the results obtained with $\Delta_s = 30 \text{ MHz}$ for which a fair agreement with experimental data is obtained. These simulations illustrate how the weaker hyperfine interaction with ^{10}B leads to a similar width of the hyperfine lines despite a higher nuclear spin.

We now study the spin coherence properties of V_B^- defects hosted in monoisotopic hBN crystals. To this end, Rabi oscillations were first recorded by using the experimental sequence shown in Fig. 3(a). After applying a first laser pulse to polarize the V_B^- electron spin by optical pumping, coherent spin manipulation is performed by applying a resonant microwave pulse of varying duration, and the resulting spin state is finally readout optically by recording the spin-dependent PL signal. A typical Rabi oscillation of the V_B^- electron spin is shown in Fig. 3(a). This experiment provides a calibration of the

duration of the microwave pulses (π and $\pi/2$) employed in pulsed ESR measurements. The longitudinal spin relaxation time T_1 was measured by applying the usual experimental sequence sketched in Fig. 3(b). Data fitting with an exponential decay leads to $T_1 \sim 16 \mu\text{s}$ for the two monoisotopic hBN crystals. This value, which is consistent with that recently reported in the literature, is limited by the interaction of the V_{B}^- electron spin with lattice phonons [19]. A spin echo sequence was then applied to infer the spin coherence time T_2 [Fig. 3(c)]. By fitting the measured echo signal with an exponential decay, we obtain $T_2 = 46 \pm 3 \text{ ns}$ for the h^{11}BN crystal and $T_2 = 62 \pm 3 \text{ ns}$ for the h^{10}BN crystal.

The coherence time of spin defects in solids is commonly limited by the magnetic noise produced by a bath of fluctuating paramagnetic impurities, which includes electron spin impurities in the host material, dangling bonds at the sample surface and nuclear spins. To better understand the origin of the short spin coherence time observed for V_{B}^- centers in our monoisotopic hBN crystals, we first investigate the impact of the nuclear spin bath by performing numerical simulations with the generalized cluster correlation expansion method (gCCE) [35, 36]. Within this theoretical framework, one can account for decoherence effects of different levels of complexity. When considering a bath dominated by nuclear spin species, the most common sources of dephasing are (i) nuclear spin flip-flops driven by the hyperfine interaction with the central electron spin, (ii) nuclear spin flip-flops induced by nuclear spin-nuclear spin dipolar interaction, and (iii) many-body correlation effects [35, 36]. We find that all these effects up to three-nuclear spin correlation contribute to the decoherence of the V_{B}^- center in hBN. We therefore rely on the third order approximation (gCCE3) in our simulations (see Supplementary Material). In addition, we use the hyperfine coupling constants calculated in Ref. [26], which include the Fermi contact interaction. While this term is often neglected owing to the highly localized nature of the electron spin density associated with point defects in semiconductors [37], it plays an important role in the decoherence of the V_{B}^- center in hBN, as discussed below.

The simulated spin echo decay curves of the V_{B}^- center in h^{11}BN and h^{10}BN are shown in Figs. 4(a,b). Both curves are fitted with a stretched exponential function, $\exp[-(t/T_2)^n]$, leading to $T_2 = 92 \text{ ns}$ and $T_2 = 115 \text{ ns}$ for h^{11}BN and h^{10}BN , respectively, with an exponent $n \sim 1.35$. The dependence of the coherence time with the isotopic content is depicted in Fig. 4(c). It reveals a linear increase with the ^{10}B abundance. This effect results from the reduced nuclear gyromagnetic ratio of ^{10}B , that weakens the hyperfine interaction and the boron nuclear spin flip-flop rate, both of which has a positive impact on the coherence time of the central spin. The convergence of the simulation with respect to the size of the nuclear spin bath provides important additional informations on

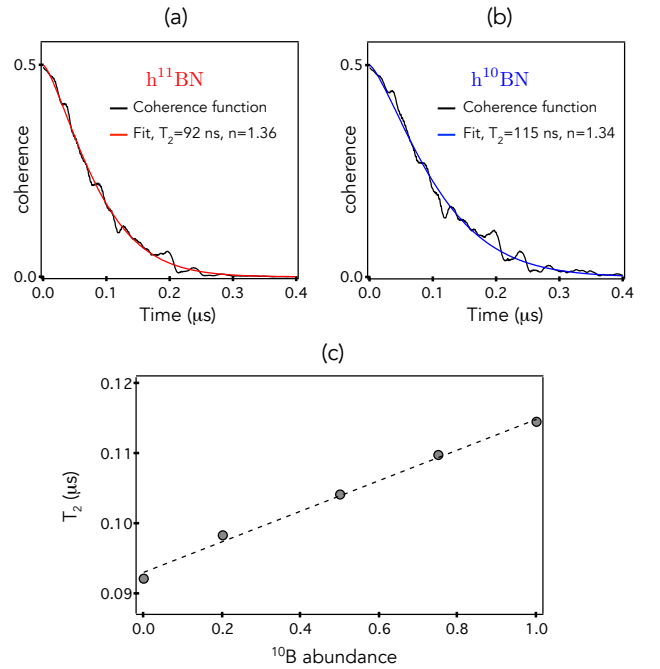


FIG. 4. **Nuclear spin bath induced decoherence.** (a,b) Simulated spin echo decay curve and corresponding stretched exponential fit for the V_{B}^- defect in (a) h^{11}BN and (b) h^{10}BN . (c) Calculated spin coherence time T_2 as a function of the abundance of ^{10}B isotope. The T_2 time is enhanced by the reduced hyperfine and nuclear spin-nuclear spin interaction strengths in ^{10}B -enriched samples. The black dashed line is a linear fit.

the decoherence processes. Indeed, our results indicate that the coherence time is mostly limited by the fluctuations of nuclear spins that are not farther than 0.8 nm from the central spin (see Supplementary Material). We thus conclude that decoherence of the V_{B}^- electron spin in a nuclear spin bath is governed by highly localized interactions. As a result, nuclear spin flip-flops driven by the hyperfine interaction, which includes both the Fermi contact and the dipolar terms, play a critical role in the decoherence process. If the contact interaction and the first order coherence contribution are neglected in the simulation, we obtain a spin coherence time up to $23 \mu\text{s}$, a value in line with earlier theoretical works [37]. The two orders of magnitude difference in the calculated coherence times, however, clearly falsifies the validity of these approximations. In fact, by taking the Fermi contact term into account, the \mathcal{A}_{zz} hyperfine term of the first and second neighbor shell atoms of the V_{B}^- center increase by a factor of ~ 28 and 2.7 , respectively. Since the phase shift induced by the nuclear spin flip-flops is determined by the \mathcal{A}_{zz} hyperfine terms, neglecting the Fermi contact has a drastic impact on the spin coherence function of all CCE orders. Furthermore, the first order CCE coherence function (C1) can solely be neglected when the Zeeman splitting of the nuclear spins exceeds

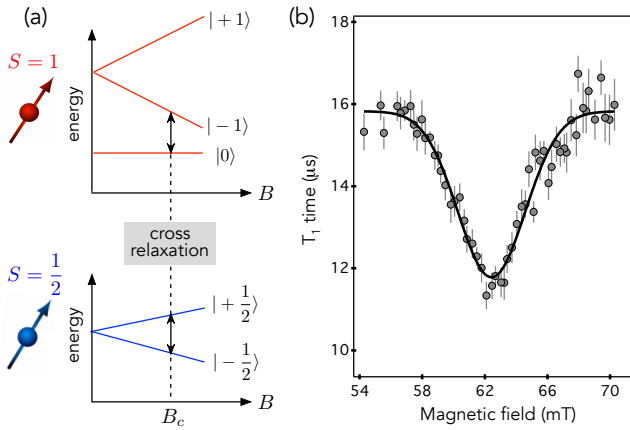


FIG. 5. **Cross-relaxation spectroscopy.** (a) Energy levels of the V_B^- spin triplet ground state (top panel) and of a paramagnetic impurity with $S = 1/2$ (bottom panel) as a function of a static magnetic field B . The two spin systems are brought in resonance for $B = B_c \sim 62$ mT. (b) T_1 time of the V_B^- spin defect in the $h^{10}\text{BN}$ crystal as a function of a magnetic field applied along the c -axis. The field amplitude is inferred by recording the Zeeman shift of the ESR frequency of the V_B^- defect. The solid line is data fitting with a Gaussian function.

the strength of the hyperfine coupling. Since the latter is the 10 MHz range for neighboring nuclear spins, the required magnetic field to suppress the first order coherence function falls far beyond reach, in the 10-100 Tesla region. These results strikingly illustrates that the Fermi contact term and the first order coherence function cannot be neglected in the calculation of the coherence properties of spin defects in hBN.

Even though our experimental results reproduce the slight increase of the spin coherence time in $h^{10}\text{BN}$, the measured T_2 values are about 50% smaller than the theoretical predictions [Fig. 3(c)]. This discrepancy could be explained by an additional source of decoherence in the experiments, such as electron spin impurities in the environment. Several paramagnetic centers with electronic spin $S = 1/2$ have been identified in neutron-irradiated hBN crystals through electron paramagnetic resonance (EPR) measurements [38–40]. Some of these defects were recently assigned to $N_B V_N$ and $C_N V_B$ centers [40]. To probe the presence of such $S = 1/2$ paramagnetic impurities in the vicinity of V_B^- centers, we measured the longitudinal spin relaxation time T_1 as a function of a static magnetic field applied along the c axis. When the ESR transition of the V_B^- center is brought in resonance with a target spin, cross-relaxation is induced by dipole-dipole interaction, which leads to a reduction of T_1 [Fig. 5(a)] [41–43]. Considering a paramagnetic center with $S = 1/2$, the resonance condition is obtained for a magnetic field $B_c = D/2\gamma_e$, where $\gamma_e = 28$ GHz/T is the electron spin gyromagnetic ratio. For the V_B^- center, it corresponds to $B_c \sim 62$ mT. The experimental results are displayed in Figure 5(b). As anticipated, a drop of

the longitudinal spin relaxation time is observed around 62 mT, which reveals the existence of dark electron spin impurities with $S = 1/2$ in the close vicinity of the V_B^- defects. The reduced value of the T_2 time in our experiments compared to theoretical predictions is attributed to fluctuations of these paramagnetic centers.

We note that the few studies found in the literature on the spin coherence properties of V_B^- centers in hBN provide very different results. In Ref. [44], a coherence time around $T_2 \sim 80$ ns was measured in a neutron-irradiated hBN samples with a natural content of boron isotopes. This value is analogous to that obtained in the present work and is supported by our theoretical predictions. On the other hand, Refs. [19, 45] have reported the observation of a few μs -long coherence time in similar hBN samples. In these studies, the contrast of the echo signal was however very weak and the experimental data at short time scale were not shown. Such long T_2 values, which are not captured by theoretical simulations using CCE methods, could be alternatively attributed to nuclear spin coherence.

To conclude, we have illustrated how hBN crystals isotopically enriched with either ^{10}B or ^{11}B can be used to identify the structure of spin defects through the analysis of their hyperfine structure. Beyond the V_B^- center studied in this work, these methods could be applied to other spin impurities in hBN, such as carbon-related defects whose microscopic structure remains unidentified [20–22, 28]. An in-depth study of the spin coherence properties of V_B^- centers indicates a slight increase of T_2 time in ^{10}B -enriched crystals, which is supported by numerical simulations using cluster correlation expansion methods. These simulations highlight the importance of the spin density distribution, the corresponding Fermi-contact hyperfine fields, and first order correlation effect for determining the coherence time of solid-state spin qubits interacting with a dense nuclear spin bath. This finding, which generally applies to any defect hosted in a solid with a high nuclear spin density, constrains the validity of prediction of spin coherence times using hypothetical defects [46]. Using cross-relaxation spectroscopy, we finally identified dark electron spin impurities as an additional source of decoherence in hBN. Although such paramagnetic impurities have a detrimental effect of the spin coherence time, they could also be turned into a useful resource for quantum sensing applications [47]. This work provides key insights into the spin relaxation dynamics of V_B^- centers in hBN, which is a promising spin defect for the future development of flexible, atomically-thin quantum sensing foils.

Acknowledgements. This work was supported by the French Agence Nationale de la Recherche under the program ESR/EquipEx+ (grant number ANR-21-ESRE-0025), the Institute for Quantum Technologies in Occi-

tanie through the project BONIQs, the European Union H2020 Quantum Flagship Program under Grant Agreement No. 820394 (ASTERIQs), and by the U.S. Department of Energy, Office of Nuclear Energy under DOE Idaho Operations Office Contract DE-AC07-051D14517 as part of a Nuclear Science User Facilities experiment. The crystal growth (J.L. and J.H.E) in this study was supported by the Materials Engineering and Processing program of the National Science Foundation, Award Number CMMI 1538127. We acknowledge the support of The Ohio State University Nuclear Reactor Laboratory and the assistance of Susan M. White, Lei Raymond Cao, Andrew Kauffman, and Kevin Herminghuyzen for the irradiation services provided. Numerical simulations (A. G and V. I.) have been performed using the resources provided by the Hungarian Governmental Information Technology Development Agency and by the Swedish National Infrastructure for Computing (SNIC) at the National Supercomputer Centre (NSC). V.I. acknowledges the support from the MTA Premium Postdoctoral Research Program and the Knut and Alice Wallenberg Foundation through WBSQD2 project (Grant No. 2018.0071). A. G. acknowledges the National Research, Development, and Innovation Office of Hungary Grant No. KKP129866 of the National Excellence Program of Quantum-Coherent Materials Project and the Quantum Information National Laboratory supported by the Ministry of Innovation and Technology of Hungary.

-
- [1] D. D. Awschalom, R. Hanson, J. Wrachtrup, and B. B. Zhou, *Nat. Phot.* **12**, 516 (2018).
- [2] G. Waldherr, Y. Wang, S. Zaiser, M. Jamali, T. Schulte-Herbruggen, H. Abe, T. Ohshima, J. Isoya, J. F. Du, P. Neumann, and J. Wrachtrup, *Nature* **506**, 204 (2014).
- [3] B. Hensen, H. Bernien, A. E. Dréau, A. Reiserer, N. Kalb, M. S. Blok, J. Ruitenber, R. F. L. Vermeulen, R. N. Schouten, C. Abellán, W. Amaya, V. Pruneri, M. W. Mitchell, M. Markham, D. J. Twitchen, D. Elkouss, S. Wehner, T. H. Taminiau, and R. Hanson, *Nature* **526**, 682 (2015).
- [4] M. Pompili, S. L. N. Hermans, S. Baier, H. K. C. Beukers, P. C. Humphreys, R. N. Schouten, R. F. L. Vermeulen, M. J. Tiggelman, L. dos Santos Martins, B. Dirkse, S. Wehner, and R. Hanson, *Science* **372**, 259 (2021).
- [5] C. L. Degen, F. Reinhard, and P. Cappellaro, *Rev. Mod. Phys.* **89**, 035002 (2017).
- [6] L. Rondin, J.-P. Tetienne, T. Hingant, J.-F. Roch, P. Maletinsky, and V. Jacques, *Reports on Progress in Physics* **77**, 056503 (2014).
- [7] R. Schirhagl, K. Chang, M. Loretz, and C. L. Degen, *Annual Review of Physical Chemistry* **65**, 83 (2014).
- [8] F. Casola, T. van der Sar, and A. Yacoby, *Nature Reviews Materials* **3**, 17088 (2018).
- [9] G. Zhang, Y. Cheng, J.-P. Chou, and A. Gali, *Applied Physics Reviews* **7**, 031308 (2020).
- [10] J. P. Tetienne, *Nature Physics* **17**, 1074 (2021).
- [11] A. J. Healey, S. C. Scholten, T. Yang, J. A. Scott, G. J. Abrahams, I. O. Robertson, X. F. Hou, Y. F. Guo, S. Rahman, Y. Lu, M. Kianinia, I. Aharonovich, and J.-P. Tetienne, [arXiv:2112.03488 \[cond-mat\]](https://arxiv.org/abs/2112.03488) (2021).
- [12] G. Cassabo, P. Valvin, and B. Gil, *Nat. Phot.* **10**, 262 (2016).
- [13] T. T. Tran, K. Bray, M. J. Ford, M. Toth, and I. Aharonovich, *Nature Nanotechnology* **11**, 37 (2016).
- [14] L. J. Martínez, T. Pelini, V. Waselowski, J. R. Maze, B. Gil, G. Cassabo, and V. Jacques, *Phys. Rev. B* **94**, 121405 (2016).
- [15] N. Chejanovsky, M. Rezai, F. Paolucci, Y. Kim, T. Rendler, W. Rouabeh, F. Favaro de Oliveira, P. Herlinger, A. Denisenko, S. Yang, I. Gerhardt, A. Finkler, J. H. Smet, and J. Wrachtrup, *Nano Lett.* **16**, 7037 (2016).
- [16] N. R. Jungwirth, B. Calderon, Y. Ji, M. G. Spencer, M. E. Flatté, and G. D. Fuchs, *Nano Letters* **16**, 6052 (2016).
- [17] A. Sajid, M. J. Ford, and J. R. Reimers, *Reports on Progress in Physics* **83**, 044501 (2020).
- [18] A. Gottscholl, M. Kianinia, V. Soltamov, S. Orlinskii, G. Mamin, C. Bradac, C. Kasper, K. Krambrock, A. Sperlich, M. Toth, I. Aharonovich, and V. Dyakonov, *Nature Materials* **19**, 540 (2020).
- [19] A. Gottscholl, M. Diez, V. Soltamov, C. Kasper, A. Sperlich, M. Kianinia, C. Bradac, I. Aharonovich, and V. Dyakonov, *Science Advances* **7**, eabf3630 (2021).
- [20] N. Mendelson, D. Chugh, J. R. Reimers, T. S. Cheng, A. Gottscholl, H. Long, C. J. Mellor, A. Zettl, V. Dyakonov, P. H. Beton, S. V. Novikov, C. Jagadish, H. H. Tan, M. J. Ford, M. Toth, C. Bradac, and I. Aharonovich, *Nature Materials* **20**, 321 (2021).
- [21] N. Chejanovsky, A. Mukherjee, J. Geng, Y.-C. Chen, Y. Kim, A. Denisenko, A. Finkler, T. Taniguchi, K. Watanabe, D. B. R. Dasari, P. Auburger, A. Gali, J. H. Smet, and J. Wrachtrup, *Nature Materials* **20**, 1079 (2021).
- [22] H. L. Stern, J. Jarman, Q. Gu, S. E. Barker, N. Mendelson, D. Chugh, S. Schott, H. H. Tan, H. Sirringhaus, I. Aharonovich, and M. Atatüre, [arXiv:2103.16494 \[cond-mat\]](https://arxiv.org/abs/2103.16494) (2021).
- [23] C. Freysoldt, B. Grabowski, T. Hickel, J. Neugebauer, G. Kresse, A. Janotti, and C. G. Van de Walle, *Rev. Mod. Phys.* **86**, 253 (2014).
- [24] L. Weston, D. Wickramaratne, M. Macko, A. Alkauskas, and C. G. Van de Walle, *Phys. Rev. B* **97**, 214104 (2018).
- [25] M. Abdi, J.-P. Chou, A. Gali, and M. B. Plenio, *ACS Photonics* **5**, 1967 (2018).
- [26] V. Ivády, G. Barcza, G. Thiering, S. Li, H. Hamdi, J.-P. Chou, Ö. Legeza, and A. Gali, *npj Computational Materials* **6**, 41 (2020).
- [27] Y. Chen and S. Y. Quek, [arXiv:2108.02019 \[cond-mat\]](https://arxiv.org/abs/2108.02019) (2021).
- [28] P. Auburger and A. Gali, *Phys. Rev. B* **104**, 075410 (2021).
- [29] S. Liu, R. He, L. Xue, J. Li, B. Liu, and J. H. Edgar, *Chemistry of Materials* **30**, 6222 (2018).
- [30] F. Cataldo and S. Iglesias-Groth, *Journal of Radioanalytical and Nuclear Chemistry* **313**, 261 (2017).
- [31] R. Cuscó, B. Gil, G. Cassabo, and L. Artús, *Phys. Rev. B* **94**, 155435 (2016).

- [32] T. Q. P. Vuong, S. Liu, A. Van der Lee, R. Cuscó, L. Artús, T. Michel, P. Valvin, J. H. Edgar, G. Cassaboais, and B. Gil, *Nature Materials* **17**, 152 (2018).
- [33] R. Cuscó, L. Artús, J. H. Edgar, S. Liu, G. Cassaboais, and B. Gil, *Phys. Rev. B* **97**, 155435 (2018).
- [34] M. V. Hauf, B. Grotz, B. Naydenov, M. Dankerl, S. Pezzagna, J. Meijer, F. Jelezko, J. Wrachtrup, M. Stutzmann, F. Reinhard, and J. A. Garrido, *Phys. Rev. B* **83**, 081304 (2011).
- [35] W. Yang and R.-B. Liu, *Phys. Rev. B* **78**, 085315 (2008).
- [36] M. Onizhuk, K. C. Miao, J. P. Blanton, H. Ma, C. P. Anderson, A. Bourassa, D. D. Awschalom, and G. Galli, *PRX Quantum* **2**, 010311 (2021).
- [37] M. Ye, H. Seo, and G. Galli, *npj Computational Materials* **5**, 44 (2019).
- [38] J. R. Toledo, D. B. de Jesus, M. Kianinia, A. S. Leal, C. Fantini, L. A. Cury, G. A. M. Sáfar, I. Aharonovich, and K. Krambrock, *Phys. Rev. B* **98**, 155203 (2018).
- [39] E. M. Huseynov, T. G. Naghiyev, A. A. Garibov, N. R. Abbasov, O. A. Samedov, R. C. Gasimov, and M. A. Bayramov, *Ceramics International* **47**, 7218 (2021).
- [40] J. R. Toledo and K. Krambrock, *Journal of Physics D: Applied Physics* **54**, 065303 (2020).
- [41] H.-J. Wang, C. S. Shin, S. J. Seltzer, C. E. Avalos, A. Pines, and V. S. Bajaj, *Nature Communications* **5**, 4135 (2014).
- [42] L. T. Hall, P. Kehayias, D. A. Simpson, A. Jarmola, A. Stacey, D. Budker, and L. C. L. Hollenberg, *Nature Communications* **7**, 10211 (2016).
- [43] J. D. A. Wood, D. A. Broadway, L. T. Hall, A. Stacey, D. A. Simpson, J.-P. Tetienne, and L. C. L. Hollenberg, *Phys. Rev. B* **94**, 155402 (2016).
- [44] W. Liu, Z. P. Li, Y. Z. Yang, S. Yu, Y. Meng, Z. A. Wang, N. J. Guo, F. F. Yan, Q. Li, J. F. Wang, J. S. Xu, Y. Dong, X. D. Chen, F. W. Sun, Y. T. Wang, J. S. Tang, C. F. Li, and G. C. Guo, [arXiv:2101.11220 \[quant-ph\]](https://arxiv.org/abs/2101.11220) (2021).
- [45] X. Gao, B. Jiang, A. E. Llacsahuanga Allcca, K. Shen, M. A. Sadi, A. B. Solanki, P. Ju, Z. Xu, P. Upadhyaya, Y. P. Chen, S. A. Bhave, and T. Li, *Nano Letters* **21**, 7708 (2021).
- [46] S. Kanai, F. J. Heremans, H. Seo, G. Wolfowicz, C. P. Anderson, S. E. Sullivan, G. Galli, D. D. Awschalom, and H. Ohno, [arXiv:2102.02986 \[quant-ph\]](https://arxiv.org/abs/2102.02986) (2021).
- [47] A. O. Sushkov, I. Lovchinsky, N. Chisholm, R. L. Walsworth, H. Park, and M. D. Lukin, *Phys. Rev. Lett.* **113**, 197601 (2014).